Acquisition of cross-polarized diffraction images and study of blurring effect by one time-delay-integration camera

He Wang,[1] Yuanming Feng,[1] Yu Sa,[1] Yuxiang Ma,[2] Jun Q. Lu,[3] and Xin-Hua Hu[2,3,*]

[1]Department of Biomedical Engineering, Tianjin University, Tianjin 300072, China
[2]WavMed Technologies Corporation, Tianjin 300072, China
[3]Departments of Physics, East Carolina University, Greenville, North Carolina 27858, USA
*Corresponding author: hux@ecu.edu

Blurred diffraction images acquired from flowing particles affect the measurement of fringe patterns and subsequent analysis. An imaging unit with one time-delay-integration (TDI) camera has been developed to acquire two cross-polarized diffraction images. It was shown that selected elements of Mueller matrix of single scatters can be imaged with pixel matching precision in this configuration. With the TDI camera, the effect of blurring on imaging of scattered light propagating along the side directions was found to be much more significant for biological cells than microspheres. Despite blurring, classification of MCF-7 and K562 cells is feasible since the effect has similar influence on extracted image parameters. Furthermore, image blurring can be useful for analysis of the correlations among texture parameters for characterization of diffraction images from single cells. The results demonstrate that with one TDI camera the polarization diffraction imaging flow cytometry can be significantly improved and angular distribution of selected Mueller matrix elements can be accurately measured for rapid and morphology-based assay of particles and cells without fluorescent labeling.   © 2015 Optical Society of America

OCIS codes: (110.1650) Coherence imaging; (050.1940) Diffraction; (170.1530) Cell analysis.

http://dx.doi.org/10.1364/AO.54.005223

1. INTRODUCTION

Optical characterization of single particles in flow attracts active research interest for its noninvasive nature and wide-ranged applications, such as identification and classification of biological cells [1,2]. It is well known that spatially resolved distribution of coherent light from a scatterer carries rich information on the particle's 3D morphology [3–10]. Detection of polarization state of the scattered light yields additional information on the scatterer's molecular profiles that can be used for cell assay and disease diagnosis [11–14]. Consequently, acquisition of multiple polarized images of coherent light scatter can lead to an effective approach to quantify 3D morphology and molecular profiles of single scatterers without the need for fluorescent labeling. We have previously developed a flow cytometry method to rapidly image coherent light by single scatterers with a microscope objective [15–19], which was further improved to acquire two cross-polarized images per scatterer using two cameras [20,21]. The method of polarization diffraction imaging flow cytometry (p-DIFC) has been shown capable of distinguishing cell lines of high similarity in their 3D morphology [21].

The design of existing p-DIFC systems with two regular CCD cameras, however, has drawbacks. First, imaging of a flowing particle during an exposure time τ can lead to blurring in acquired diffraction images. For a flow speed of $v = 5$ mm/s and $\tau = 0.5$ ms, a particle of about 10 µm in size can move over a distance of $\delta = 2.5$ µm with blurred fringe patterns. This in turn affects subsequent image analysis. We have argued that the effect of blurring is similar to all scatterers and thus could be treated as a systematic error that may not prevent classification [18,19,21]. Still, blurring needs to be investigated and reduced or eliminated eventually to increase the throughput rate and robustness of the p-DIFC method [16,22]. Second, the use of two cameras presents a bottle-neck to data communication that is critical for increasing the throughput rate. Finally, imaging by two cameras always presents difficulty for aligning the fields of view with compromised system stability. In this report, we present a new design for acquiring cross-polarized diffraction images with one time-delay-integration (TDI) CCD camera. Motion blurring in cross-polarized diffraction images has been measured with the TDI camera on microspheres and biological cells. The parameters extracted

from the diffraction images acquired at different v were used to quantify blurring caused by the mismatch of flow speed and line transfer speed of the TDI camera.

2. METHODS

A. Imaging Unit and Flow Cytometer

A Wollaston prism (LSP-3A14, Laser Institute, QFNU) was incorporated in the design of a new imaging unit to separate elastically scattered light from the imaged particle according to polarization. As shown in Fig. 1(A), the two linearly polarized output beams with one polarized along the y-axis (s-polarized) and one along the z-axis (p-polarized), are separated by an angle of 20° and focused onto the same TDI sensor by taking advantage of the larger width of the sensor by a tube lens of focal length $F = 75$ mm. With TDI sensing, the unit enables imaging without blurring by adjusting the line transfer frequency of pixels to synchronize pixel line transfer and the moving image on the sensor [23], which has been employed in conventional flow cytometry for imaging noncoherent fluorescent light from moving cells [24,25]. Even though TDI cameras are commercially available, we decided to develop one for full control of various aspects of image acquisition to investigate the effect of blurring on diffraction imaging in off-focus or nonconjugate configurations [15,26].

The fluidics and light sources of the p-DIFC system have been described in detail elsewhere [16,19–21]. Briefly, a syringe pump is employed to control the flow rate of the core fluid moving the scatterers along the y-axis and an air pressure pump to control the sheath fluid for hydrodynamic focusing. A glass tubing of 120 μm inside diameter injects the core fluid into a flow chamber with a square channel of 3 mm in side length. A cw laser of 532 nm in wavelength is focused by a combination of two cylindrical lenses of 500 and 60 mm focal lengths on the core fluid inside the flow chamber in an elliptical spot with major diameter of about 300 μm along the y-axis and minor diameter of about 50 μm along the x-axis. The incident beam
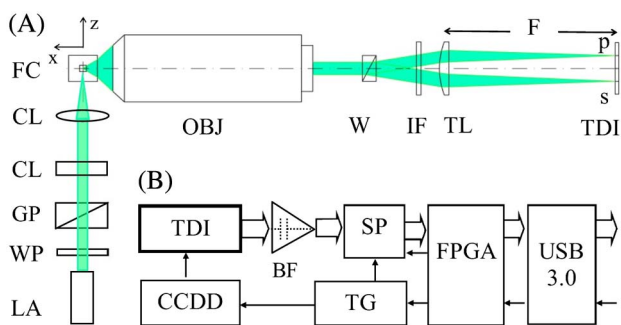

Fig. 1. (A) Top view of the imaging unit: LA, laser; WP, half-wave plate; GP, Glan–Thompson prism; CL, cylindrical lenses; FC, flow chamber; OBJ, objective; WP, Wollaston prism; IF, 532 nm interference filter; TL, tube lens; TDI, TDI sensor and camera. The green shaded lines indicate the incident laser beam (with slight different hue) and scattered light from the flow chamber FC with polarization states given by p and s. (B) The block diagram of the TDI camera: CCDD, CCD driver; BF, buffer; SP, signal processor; TG, timing generator. Single and double arrow lines indicate respectively the flows of control signal and pixel signals.

propagates along the z-axis with a linear polarization along the x-axis or p-polarized. The incident beam power was controlled by rotating the half-wave plate and measured after the second cylindrical lens, which was set to 50 mW for imaging microspheres and 70 mW for cells. The variation of the incident beam power was to avoid pixel saturation by scattered light that is stronger for microspheres of larger index mismatch than that of cells from the host medium of water. Figure 1(A) presents the top view of the optical configuration in the x–z plane.

B. Development of TDI-CCD Camera

A TDI sensor (S10201-04, Hamamatsu) of 128×2048 pixels and maximum line transfer frequency $f_{max} = 50$ kHz was selected for camera development. Different from a regular CCD sensor, the TDI's line transfer frequency f is controlled externally for synchronization with the moving image. Once achieved, a pixel line becomes "fixed" to its matching image line during line transfer until it reaches the readout shift register of the sensor. The frequency f is determined by a vertical clock pulse train from a field-programmable gate array (FPGA) and timing generator device, shown in Fig. 1(B). After it is moved into the readout register, the pixel charges are transferred horizontally as an analog output pulse train to a signal buffer and a processor which outputs digitized 12-bit pixel values to the FPGA memory. The FPGA software checks the maximum pixel values $I_{m,max}$ for each stored pixel line m and, if larger than a threshold, transfers 512 consecutive pixel lines via USB to the host computer as the acquired images. Values of f and v were adjusted respectively through software or sheath fluid pressure. For this study, the actual charge transfer takes less than 1 μs. Thus, pixels utilize nearly all of the line transfer period equal to $1/f$, 20 μs or longer, to accumulate photoelectron charges before moving to the next line, which yields an effective exposure time of the 128-line sensor as $\tau = 128/f$. For $f \le f_{max}$, τ can be 2.56 ms or longer.

C. Sample Preparation

Two types of polystyrene microspheres have been used for this study with nominal diameter of $d = 9.6$ μm (No. 7510A, Duke Scientific) and 5.7 μm (No. 6-1-0500, Tianjin Baseline ChromTech Research Centre). The MCF-7 and K562 cells derived from human breast carcinoma and chronic myelogenous leukemia (ATCC, Manassas, VA) have been investigated. The two cell lines were maintained in the RPMI 1640 culture medium supplemented with 10% fetal bovine serum at the Tianjin University of Medicine (TJMU). The adherent MCF-7 cells were removed from culture flask with trypsin-EDTA to suspend cells in culture medium as the sample before each measurement.

3. RESULTS AND DISCUSSION

Before the start of a measurement, the imaging unit was first aligned relative to the flow chamber to a focused position denoted as $\Delta x = 0$, at which the core fluid can be clearly observed on the object plane of the objective under white light illumination. Then the imaging unit was translated toward the flow chamber to an off-focused position of $\Delta x = 220$ μm for acquiring diffraction images with the incident laser beam and the white light source turned off. The off-focus imaging of

coherent light from the scatterer with the objective has been shown to be the key for acquiring diffraction images of high contrast [15,26].

A. Microspheres

Figure 2 presents four examples of the acquired diffraction images of 2048 x 512 pixels by one TDI camera with $f = 16.67$ kHz, $\lambda = 532$ nm, and $v = 10.6$ mm/s. Each image consists of two portions with the left half displaying the spatial or angular distribution of the s-polarized scattered light and the right half of the p-polarized light. It can be seen that the coherent light scattered by the two microspheres present no s-polarized scattered light in the left halves of the images while the cells present weak but nonzero s-polarized scattered light in the same part of the images. In contrast, all diffraction images present strong p-polarized scattered light in the right halves, which is limited within a circular aperture due to the exit pupil of objective [26].

To validate the new imaging design and illustrate its future use for measurement of certain Mueller matrix elements [13], one can apply the Mueller–Stokes formulism and Mie theory for understanding the distribution of cross-polarized light scatter shown in Fig. 2. For single particles of unknown morphology excited with a coherent incident beam of p-polarization, the Stokes vectors of p- and s-polarized scattered light denoted as I_{jp} with $j = p$ or s can be found as [3]

$$I_{jp} = \begin{pmatrix} S_{11} + S_{12} \pm S_{21} \pm S_{22} \\ \pm S_{11} \pm S_{12} + S_{21} + S_{22} \\ 0 \\ 0 \end{pmatrix}$$

$$= \begin{pmatrix} 1 & \pm 1 & 0 & 0 \\ \pm 1 & 1 & 0 & 0 \\ 0 & 0 & 0 & 0 \\ 0 & 0 & 0 & 0 \end{pmatrix} \begin{pmatrix} S_{11} & S_{12} & S_{13} & S_{14} \\ S_{21} & S_{22} & S_{23} & S_{24} \\ S_{31} & S_{32} & S_{33} & S_{34} \\ S_{41} & S_{42} & S_{43} & S_{44} \end{pmatrix} \begin{pmatrix} 1 \\ 1 \\ 0 \\ 0 \end{pmatrix}, \tag{1}$$

where the first matrix on the second line of the above equation represents the polarization selection capability of the Wollaston prism with $+1$ for $j = p$ and -1 for $j = s$ and the middle one is for the single scatterer. For a microsphere, only eight elements of its Mueller matrix are nonzero and related to each other by $S_{22} = S_{11}$, $S_{21} = S_{12}$, $S_{44} = S_{33}$, and $S_{43} = -S_{34}$. Obviously, the s-polarized portions of the diffraction images by microspheres are expected to be null according to Eq. (1) since $S_{11} + S_{12} - S_{21} - S_{22} = 0$ for the measured first element of the Stokes vector I_{sp}. But for particles
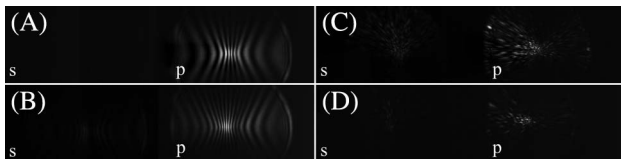
of complex and nonspherical morphology such as the cells, the corresponding element of I_{sp} is in general nonzero, whose angular distribution, and that of the first element of I_{pp}, depend on the 3D distribution of refractive index inside the particle relative to that of the host medium [3,8].

It is worth noting that the first element values of the Stokes vectors I_{pp} and I_{sp} provide the scattered light intensity at a specific direction defined by the polar and azimuthal scattering angles, or proportional to the pixel values in the p- or s-polarized portions, respectively. The results shown in Fig. 2 thus demonstrate that the new design with one camera to image scattered light of cross polarizations could be used in the future to measure angle-resolved distribution of certain combinations of the Mueller matrix elements. Use of one camera has the advantage of pixel matching precision achieved by rotating the Wollaston prism only around the optical axis of the imaging unit or the x-axis. We also note that the present design can be varied with different polarization selecting devices for the incident beam [21] to acquire additional polarized and pixel-matched images and determine other Mueller matrix elements or linear combinations of elements. Because of the slow detection with exposure time of the order of milliseconds, however, the imaging approach shown here does not have the capacity to determine all of the Mueller matrix elements using the polarization modulation technique and fast detector [13].

For the following discussion of the blurring effect, we only need to study one polarized portion of an acquired image data of 2048 × 512 pixels by the TDI camera. Therefore, we will present in the rest of the report only the p-polarized portions of the acquired diffraction images cropped out of raw images of 400 × 200 pixels as the p-polarized diffraction images because these present high contrast due to the p-polarization of the incident laser beam. These images are centered to the circular aperture that can be clearly seen in Figs. 2(A) and 2(B).

Figure 3(A) presents three p-polarized diffraction images acquired from single microspheres of $d = 9.6$ μm at different flow speed v, which was determined from the shadow of microspheres illuminated with a noncoherent light beam and imaged by a regular CCD camera set at $\Delta x = 0$ with a magnification of 18.75 and an exposure time of 3 ms. When v was set at $v_m = 10.6$ mm/s and the line transfer frequency f set at
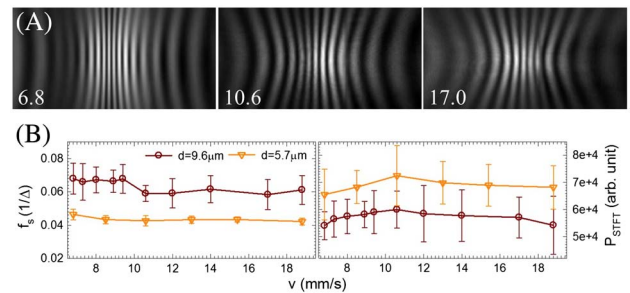

Fig. 2. s- and p-polarized diffraction images of (A) one microsphere of diameter $d = 5.7$ μm; (B) one microsphere of $d = 9.6$ μm; (C) one MCF-7 cell; (D) one K562 cell. The letters at the bottom of each image potion indicate the polarization states of the scattered light separated by the Wollaston prism.

Fig. 3. (A) p-polarized diffraction images of three microspheres of $d = 9.6$ μm with v given in mm/s; (B) dependence of center frequency f_s and amplitude PSTFT(fs) on v for two types of microspheres. The symbols and error bars represent the mean values and standard deviations obtained from 30 to 40 microspheres and lines are for visual guide.

$f_m = 16.6$ kHz, the least amount of blurring can be observed in the diffraction images of the biological cells. The synchronization achieved with v_m and f_m has been verified by determination of the speed of moving image from v_m and magnification of the imaging unit. The value of f_m was chosen to keep minimal background noise of the TDI sensor pixels at 3% or less of the full scale of the pixel values.

The algorithm of 1D short-time-Fourier-transform (STFT) has been applied on diffraction images of microspheres [19]. The STFT algorithm accounts for the variation of period of fringe patterns in an image by performing Fourier transforms within a window of width w. For the images considered here, we chose $w = 90\Delta$ with Δ as pixel distance to obtain a well-defined sideband in the STFT power spectrum of the center row in each image beside the DC background peak, which is characterized by a peak frequency f_s and the amplitude $P_{\text{STFT}}(f_s)$. Figure 3(B) shows the plots of f_s and P_{STFT} against v. These results indicate that the blurring affects very little on the periodic arrangement of the fringes in the images and consequently f_s because the directions of the core flow and the pixel columns in Fig. 3(A) are both along the y-axis against which the fringe patterns are formed. Still the synchronization of the TDI sensor line transfer with the particles flowing at $v_m = 10.6$ mm/s increases the image contrast and thus the amplitude P_{STFT} at v_m for both types of the microspheres.

B. Biological Cells
Compared to microspheres, the diffraction images of biological cells exhibit little symmetry in their fringe patterns. These images become severely blurred, as shown in Fig. 4(A), for large mismatch in motion between the imaged particle and line pixel charges of the camera. Based on our previous studies, we employed the gray level co-occurrence matrix (GLCM) algorithm to extract 15 parameters to examine quantitatively their
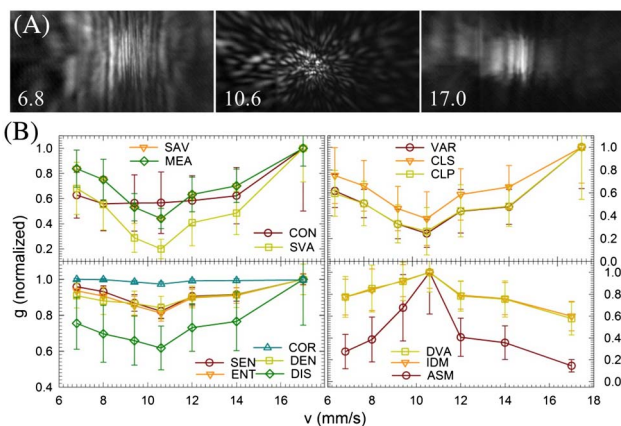
dependence on mismatch as the markers investigation of the blurring effect on image texture, as plotted in Fig. 4(B) [18,27].

The data in Figs. 4 and 5 show clearly that the blurring affects significantly the GLCM parameters and the blur-free imaging at v_m can significantly improve the accuracy of image analysis and subsequent cell assay. It is interesting to note that blurring creates artificial texture patterns convoluted with the diffraction fringes. As a result, data in Figs. 4(B) and 5(A) provide an intriguing test on correlations among those GLCM parameters exhibiting similar v dependence. For example, the v dependence of the normalized GLCM parameters reveals that MEA and SAV as a group and VAR, CLS, and CLP as a group (see Fig. 4 caption) exhibit identical or highly similar variations. The measured similarities suggest that the abstract GLCM parameters in each group characterize image textures or patterns alike and thus imaging with controllable blurring provides an experimental approach to investigate the correlations among the GLCM parameters in addition to inference based on their definitions [27]. We are currently extending this study with additional diffraction image data from other cell types.

To illustrate the blurring effect on cell classifications, we performed measurement with K562 cells for comparison with MCF-7 cells under identical flow and imaging conditions. Figure 5 presents selected examples of the GLCM parameters extracted from the p-polarized diffraction images as function of flow speed v with fixed line transfer frequency f. The 3D scatter plots of three GLCM parameters in Fig. 5(B) clearly demonstrate that the two cell lines can be distinguished satisfactorily into two clusters when $v = v_m$. As v deviates from v_m the two cell lines start to have certain degrees of mixing, as shown by the right scatter plot in Fig. 5(B). Still, even for certain cases of $v \neq v_m$, the two groups of cells can still be distinguished in the space of multiple GLCM parameters using machine learning algorithms, such as support vector machine (SVM) with additional GLCM parameters [21,28].
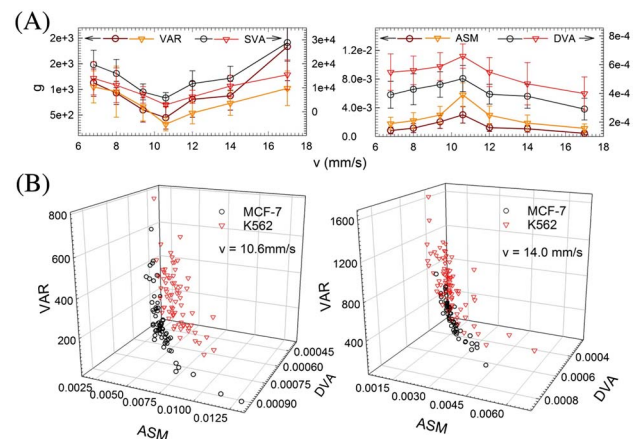

Fig. 4. (A) p-polarized diffraction images of three MCF-7 cells with v in mm/s; (B) dependence of normalized GLCM parameters g on v for MCF-7 cells: SAV, sum average; MEA, mean; CON, contrast; SVA, sum variance; SEN, sum entropy; ENT, entropy; COR, correlation; DEN, difference entropy; DIS, dissimilarity; VAR, variance; CLS, cluster shade; CLP, cluster prominence; DVA, difference variance; IDM, inverse difference moment; ASM, angular second moment. The symbols and error bars represent the mean values and standard deviations obtained from 50 to 100 cells and lines are for visual guide.

Fig. 5. (A) Dependence of GLCM parameters g on v for MCF-7 cells (circle symbols) and K562 cells (triangle symbols). The lines are for visual guide. (B) Scatter plots in the 3D GLCM parameter space of MCF-7 and K562 cells at different values of v, the left plot contains 62 MCF-7 and 64 K562 cells and the right plot contains 74 and 88 cells, respectively.

With a previously developed classification software based on the SVM algorithm, we have obtained classification accuracy A for the data shown in Fig. 5 [21]. Five tests of classification were performed on the data employed as the training data for the three selected GLCM parameters with one of four kernel functions and an iterating scheme of fivefold cross validation. The values of A were found to range from 96% to 83% in the case of $v = 10.6$ mm/s, which reduced to, respectively, from 89% to 67% in the case of $v = 14.0$ mm/s with different kernel functions of linear, polynomial, Gaussian radial basis function, and sigmoid [28]. We should point out that the classification performance of algorithms such as SVM relies on the size of training data and the values of A are expected to increase with the number of cells in the two cell samples used as the training data. Thus, blurring may reduce the robustness of cell classification by adding experimental errors but does not always prevent classification and the effect may be compensated by using a large training dataset, as demonstrated by our previous study on classification of Jurkat and Ramos cells using regular CCD cameras [21]. It should be noted that blurring can lead to the disappearance of differences in GLCM parameters between different cell types, as shown by the case of VAR when v is less than v_m. Furthermore, the effect of blurring can become much more significant in cases of classifying cell types with morphological similarity much higher than the case shown here.

Compared to the conventional methods of cell classification based on morphology, such as fluorescence microscopy [29], the *p*-DIFC method reported in previous and this report provides similar classification accuracies that can be higher than 90% for a large training dataset [21] or a small training dataset with blurring reduced or eliminated as shown here. Unlike conventional microscopy images acquired with incoherent light, analysis of diffraction images requires no segmentation and can be automated with existing algorithms of texture analysis such as GLCM. With the advantages of label-free and rapid analysis, the p-DIFC method has the potential to yield an efficient approach for assay and profiling of single biological cells with minimal disturbance.

4. CONCLUSION

We have developed a new imaging method to acquire two cross-polarized diffraction images from single scatterers with one TDI camera. The capability of the new method has been demonstrated for measurement and determination of the spatial distribution of certain combinations of Mueller matrix elements for a scatterer within an angular range, which can be applied to perform morphology-based analysis of the scatterers. It has been shown that blurring affects severely the diffraction patterns of cells with low degree of symmetry in their morphology but may not prevent classification of certain cell types.

REFERENCES

1. C. E. Pedreira, E. S. Costa, M. E. Arroyo, J. Almeida, and A. Orfao, "A multidimensional classification approach for the automated analysis of flow cytometry data," IEEE Trans. Biomed. Eng. **55**, 1155–1162 (2008).
2. C. Tropea, "Optical particle characterization in flows," Annu. Rev. Fluid Mech. **43**, 399–426 (2011).
3. C. F. Bohren and D. R. Huffman, *Absorption and Scattering of Light by Small Particles* (Wiley, 1983), p. 65.
4. M. H. Maleki, A. J. Devaney, and A. Schatzberg, "Tomographic reconstruction from optical scattered intensities," J. Opt. Soc. Am. A **9**, 1356–1363 (1992).
5. A. Dunn, C. Smithpeter, A. J. Welch, and R. Richards-Kortum, "Finite-difference time-domain simulation of light scattering from single cells," J. Biomed. Opt. **2**, 262–266 (1997).
6. S. Holler, Y. Pan, R. K. Chang, J. R. Bottiger, S. C. Hill, and D. B. Hillis, "Two-dimensional angular optical scattering for the characterization of airborne microparticles," Opt. Lett. **23**, 1489–1491 (1998).
7. J. Neukammer, C. Gohlke, A. Hope, T. Wessel, and H. Rinneberg, "Angular distribution of light scattered by single biological cells and oriented particle agglomerates," Appl. Opt. **42**, 6388–6397 (2003).
8. J. Q. Lu, P. Yang, and X. H. Hu, "Simulations of light scattering from a biconcave red blood cell using the FDTD method," J. Biomed. Opt. **10**, 024022 (2005).
9. R. S. Brock, X. H. Hu, D. A. Weidner, J. R. Mourant, and J. Q. Lu, "Effect of detailed cell structure on light scattering distribution: FDTD study of a B-cell with 3D structure constructed from confocal images," J. Quant. Spectrosc. Radiat. Transfer **102**, 25–36 (2006).
10. D. I. Strokotov, A. E. Moskalensky, V. M. Nekrasov, and V. P. Maltsev, "Polarized light-scattering profile—advanced characterization of nonspherical particles with scanning flow cytometry," Cytometry A **79A**, 570–579 (2011).
11. V. Backman, R. Gurjar, K. Badizadegan, I. Itzkan, R. R. Dasari, L. T. Perelman, and M. Feld, "Polarized light scattering spectroscopy for quantitative measurement of epithelial cellular structures in situ," IEEE J. Sel. Top. Quantum Electron. **5**, 1019–1026 (1999).
12. L. Liu, R. Oldenbourg, J. R. Trimarchi, and D. L. Keefe, "A reliable, noninvasive technique for spindle imaging and enucleation of mammalian oocytes," Nat. Biotechnol. **18**, 223–225 (2000).
13. H. Ding, J. Q. Lu, R. S. Brock, T. J. McConnell, J. F. Ojeda, K. M. Jacobs, and X. H. Hu, "Angle-resolved Mueller matrix study of light scattering by B-cells at three wavelengths of 442, 633 and 850 nm," J. Biomed. Opt. **12**, 034032 (2007).
14. A. Pierangelo, A. I. Benali, M.-R. Antonelli, T. Novikova, P. Validire, B. Gayet, and A. De Martino, "Ex-vivo characterization of human colon cancer by Mueller polarimetric imaging," Opt. Express **19**, 1582–1593 (2011).
15. K. M. Jacobs, L. V. Yang, J. Ding, A. E. Ekpenyong, R. Castellone, J. Q. Lu, and X. H. Hu, "Diffraction imaging of spheres and melanoma cells with a microscope objective," J. Biophotonics **2**, 521–527 (2009).
16. K. M. Jacobs, J. Q. Lu, and X. H. Hu, "Development of a diffraction imaging flow cytometer," Opt. Lett. **34**, 2985–2987 (2009).
17. X. Su, S. E. Kirkwood, M. Gupta, L. Marquez-Curtis, Y. Qiu, A. Janowska-Wieczorek, W. Rozmus, and Y. Y. Tsui, "Microscope-based label-free microfluidic cytometry," Opt. Express **19**, 387–398 (2011).
18. K. Dong, Y. Feng, K. M. Jacobs, J. Q. Lu, R. S. Brock, L. V. Yang, F. E. Bertrand, M. A. Farwell, and X. H. Hu, "Label-free classification of cultured cells through diffraction imaging," Biomed. Opt. Express **2**, 1717–1726 (2011).
19. Y. Sa, J. Zhang, M. S. Moran, J. Q. Lu, Y. Feng, and X. H. Hu, "A novel method of diffraction imaging flow cytometry for sizing microspheres," Opt. Express **20**, 22245–22251 (2012).
20. J. Zhang, Y. Feng, M. S. Moran, J. Q. Lu, L. V. Yang, Y. Sa, N. Zhang, L. Dong, and X. H. Hu, "Analysis of cellular objects through diffraction images acquired by flow cytometry," Opt. Express **21**, 24819–24828 (2013).
21. Y. Feng, N. Zhang, K. M. Jacobs, W. Jiang, L. V. Yang, Z. Li, J. Zhang, J. Q. Lu, and X. H. Hu, "Polarization imaging and classification of

Jurkat T and Ramos B cells using a flow cytometer," Cytometry A **85**, 817–826 (2014).

22. Y. Sa, Y. Feng, K. M. Jacobs, J. Yang, R. Pan, I. Gkigkitzis, J. Q. Lu, and X. H. Hu, "Study of low speed flow cytometry for diffraction imaging with different chamber and nozzle designs," Cytometry A **83**, 1027–1033 (2013).

23. D. F. Barbe, "Imaging devices using the charge-coupled concept," Proc. IEEE **63**, 38–67 (1975).

24. S. H. Ong, D. Horne, C. K. Yeung, P. Nickolls, and T. Cole, "Development of an imaging flow cytometer," Anal. Quant. Cytol. Histol. **9**, 375–382 (1987).

25. T. C. George, D. A. Basiji, B. E. Hall, D. H. Lynch, W. E. Ortyn, D. J. Perry, M. J. Seo, C. A. Zimmerman, and P. J. Morrissey,

"Distinguishing modes of cell death using the ImageStream multispectral imaging flow cytometer," Cytometry A **59**, 237–245 (2004).

26. R. Pan, Y. Feng, Y. Sa, J. Q. Lu, K. M. Jacobs, and X. H. Hu, "Analysis of diffraction imaging in non-conjugate configurations," Opt. Express **22**, 31568–31574 (2014).

27. R. M. Haralick, "Statistical and structural approaches to texture," Proc. IEEE **67**, 786–804 (1979).

28. C. C. Chang and C. J. Lin, "LIBSVM: a library for support vector machines," ACM Trans. Intell. Syst. Technol. **2**, 1–27 (2011).

29. X. Chen, X. Zhou, and S. T. C. Wong, "Automated segmentation, classification, and tracking of cancer cell nuclei in time-lapse microscopy," IEEE Trans. Biomed. Eng. **53**, 762–766 (2006).